Author(s): Hinkkanen, Marko & Qu, Zengcai & Awan, Hafiz Asad Ali & Tuovinen, Toni & Briz, Fernando

Title: Current control for IPMSM drives: Direct discrete-time pole-placement design

Year: 2015

Version: Post print

Please cite the original version:

Hinkkanen, Marko & Qu, Zengcai & Awan, Hafiz Asad Ali & Tuovinen, Toni & Briz, Fernando. 2015. Current control for IPMSM drives: Direct discrete-time pole-placement design. IEEE Workshop on Electrical Machines Design, Control and Diagnosis (WEMDCD). 9. ISBN 978-1-4799-8900-3 (electronic). DOI: 10.1109/wemdcd.2015.7194524.

Current Control for IPMSM Drives: Direct Discrete-Time Pole-Placement Design

Marko Hinkkanen*, Zengcai Qu*, Hafiz Asad Ali Awan*, Toni Tuovinen†, and Fernando Briz‡
*Aalto University, Espoo, Finland
†ABB Drives, Helsinki, Finland
‡University of Oviedo, Gijón, Spain

***Abstract*—This paper deals with discrete-time models and current control methods for synchronous motors with a magnetically anisotropic rotor structure, such as interior permanent-magnet synchronous motors (IPMSMs) and synchronous reluctance motors (SyRMs). Dynamic performance of current controllers based on continuous-time models is limited, especially if the ratio of the sampling frequency to the fundamental frequency is low. An exact closed-form hold-equivalent discrete motor model is derived. The zero-order hold of the stator-voltage input is modeled in stationary coordinates, where it physically is. An analytical discrete-time pole-placement design method for a two-degree-of-freedom state-space current controller with an integral action is proposed. The proposed method is easy to apply: only the desired closed-loop bandwidth and the three motor parameters (R_s, L_d, L_q) are required. The robustness of the proposed current control design against parameter errors is analyzed. The controller is experimentally verified using a 6.7-kW SyRM drive.**

***Index Terms*—Current control, delay, discrete-time model, interior permanent-magnet synchronous motor (IPMSM), synchronous reluctance motor (SyRM), zero-order hold.**

I. Introduction

Synchronous motors with a magnetically anisotropic rotor—such as interior permanent-magnet synchronous motors (IPMSMs), synchronous reluctance motors (SyRMs), and permanent-magnet-assisted SyRMs—are more and more applied in hybrid (or electric) vehicles, heavy-duty working machines, and industrial applications. In these applications, the maximum speeds and, consequently, the maximum operating frequencies can be very high (e.g., 12 000 r/min corresponding to the frequency of 1 000 Hz for a ten-pole machine). Since the switching frequency of the converter feeding the motor is limited due to the losses, the resulting ratio between the switching frequency and the maximum fundamental frequency can be even below ten. This will affect the sampling frequency, too, as it is typically equal to or twice the switching frequency.

Generally, the stator current of synchronous motor drives is controlled in rotor coordinates [1]–[11]. This coordinate system is a natural selection since the controllable quantities are DC in steady state, the inductance matrix and the PM-flux vector are (ideally) constant, and other parts of the control system typically operate in rotor coordinates. The most widely used current control approach is to use a synchronous-frame proportional-integral (PI) controller, often augmented with decoupling terms to compensate for the cross-coupling due to the rotating coordinate system. Typically, the controller is first designed in the continuous-time domain and then discretized for the digital implementation using, e.g., the Euler or Tustin approximation [1]–[5]. This approach is well understood and works well in most applications. However, the closed-loop control bandwidth and the maximum operating frequency are limited to below approximately 5% of the sampling frequency. Furthermore, heuristic compensations for the angular errors due to time delays are often needed. Higher dynamic performance at a given sampling frequency could be achieved by designing the controller directly in the discrete-time domain [6], [8]–[11].

A hold-equivalent discrete model—including the effects of the zero-order hold (ZOH) and a sampler—of the motor drive is needed for the direct discrete-time control design. An exact closed-form hold-equivalent model has been derived for induction motor drives in [12] and an approximate discrete model for the IPMSM drives has been proposed in [9], [10]. The exact closed-form hold-equivalent model for surface permanent-magnet synchronous motor (SPMSM) drives can be found in [6], [8], but the closed-form expressions valid for IPMSM drives are not available in the literature.

In this paper, current control designs based on discrete IPMSM models are considered. First, the motor model and the control design in the continuous-time domain are reviewed in Section II. Then, the main results are presented as follows.

1) An exact closed-form hold-equivalent discrete model for IPMSM drives is derived in Section III. The ZOH of the stator-voltage input is modeled in stationary coordinates, where it physically is. The model provides the mapping between the continuous-time model (with physical parameters) and the discrete-time model. The derived closed-form expressions can be applied to the design, analysis, and implementation of controllers and observers (e.g., in connection with deadbeat [13] or predictive [14] direct torque control methods).
2) An analytical direct discrete-time pole-placement design method for a two-degree-of-freedom (2DOF) state-space current controller with an integral action is proposed in Section IV. The time delays are inherently taken into account in the design. The proposed method is easy to apply: only the desired closed-loop bandwidth and the three motor parameters are needed.
3) The robustness of the proposed current control design against parameter errors is analyzed in Section V. The operation of the controller is further investigated by means of simulations and experiments using a 6.7-kW SyRM drive.

Naturally, the model and the control design method are directly applicable to SPMSM drives as well.

II. Continuous-Time Model and Control Design

A. Continuous-Time Model

In order to model IPMSMs, real space vectors will be used throughout the paper. For example, the stator-current vector is $\boldsymbol{i}_\mathrm{s} = [i_\mathrm{d}, i_\mathrm{q}]^\mathrm{T}$, where i_d and i_q are the components of the vector and the matrix transpose is marked with the superscript T. The identity matrix, the orthogonal rotation matrix, and the zero matrix are defined, respectively, as[1]

$$\boldsymbol{I} = \begin{bmatrix} 1 & 0 \\ 0 & 1 \end{bmatrix}, \quad \boldsymbol{J} = \begin{bmatrix} 0 & -1 \\ 1 & 0 \end{bmatrix}, \quad \boldsymbol{O} = \begin{bmatrix} 0 & 0 \\ 0 & 0 \end{bmatrix} \tag{1}$$

Vectors are denoted using boldface lowercase letters and matrices using boldface uppercase letters. Space vectors in stator coordinates are marked with the superscript "s", no superscript is used for space vectors in rotor coordinates.

The electrical angular speed and angle of the rotor are denoted by ω_m and $\vartheta_\mathrm{m}(t) = \int \omega_\mathrm{m} \mathrm{d}t$, respectively. The time dependency of the variables is denoted by the argument t. It is worth noticing that the rotor speed and the motor parameters will be considered as quasi-constant parameters, when the continuous-time model is discretized.

In rotor coordinates, the state-space representation corresponding to the standard model of the IPMSM is

$$\frac{\mathrm{d}\boldsymbol{\psi}_\mathrm{s}(t)}{\mathrm{d}t} = \boldsymbol{A}\boldsymbol{\psi}_\mathrm{s}(t) + \boldsymbol{B}\boldsymbol{u}_\mathrm{s}(t) + \boldsymbol{b}\psi_\mathrm{pm} \tag{2a}$$

$$\boldsymbol{i}_\mathrm{s}(t) = \boldsymbol{C}\boldsymbol{\psi}_\mathrm{s}(t) + \boldsymbol{d}\psi_\mathrm{pm} \tag{2b}$$

where $\boldsymbol{\psi}_\mathrm{s}$ is the stator flux vector, $\boldsymbol{u}_\mathrm{s}$ is the stator voltage vector, and ψ_pm is the permanent-magnet (PM) flux. The system matrices are

$$\boldsymbol{A} = \begin{bmatrix} -R_\mathrm{s}/L_\mathrm{d} & \omega_\mathrm{m} \\ -\omega_\mathrm{m} & -R_\mathrm{s}/L_\mathrm{q} \end{bmatrix}, \quad \boldsymbol{B} = \boldsymbol{I}, \quad \boldsymbol{b} = \begin{bmatrix} R_\mathrm{s}/L_\mathrm{d} \\ 0 \end{bmatrix}$$
$$\boldsymbol{C} = \begin{bmatrix} 1/L_\mathrm{d} & 0 \\ 0 & 1/L_\mathrm{q} \end{bmatrix}, \quad \boldsymbol{d} = \begin{bmatrix} -1/L_\mathrm{d} \\ 0 \end{bmatrix} \tag{3}$$

where R_s is the stator resistance, L_d is the direct-axis inductance, and L_q is the quadrature-axis inductance. The state-space representation in (2) has two inputs: the stator voltage $\boldsymbol{u}_\mathrm{s}(t)$ and the PM flux ψ_pm (which is constant). If $L_\mathrm{d} = L_\mathrm{q}$, the model represents the SPMSM. If $\psi_\mathrm{pm} = 0$, the model of the SyRM is obtained.

The model (2) can be expressed in the Laplace domain as

$$\boldsymbol{i}_\mathrm{s}(s) = \boldsymbol{Y}_\mathrm{c}(s)\left[\boldsymbol{u}_\mathrm{s}(s) - \boldsymbol{u}_\mathrm{i}(s)\right] \tag{4}$$

where the transfer-function matrix is

$$\boldsymbol{Y}_\mathrm{c}(s) = \boldsymbol{C}(s\boldsymbol{I} - \boldsymbol{A})^{-1} = \begin{bmatrix} R_\mathrm{s} + sL_\mathrm{d} & -\omega_\mathrm{m}L_\mathrm{q} \\ \omega_\mathrm{m}L_\mathrm{d} & R_\mathrm{s} + sL_\mathrm{q} \end{bmatrix}^{-1} \tag{5}$$

[1]The notation is very similar to that obtained for complex space vectors: the rotation matrix $\boldsymbol{J}$ corresponds to the imaginary unit j and the coordinate transformation matrices can be expressed using matrix exponentials, i.e., $\mathrm{e}^{\vartheta\boldsymbol{J}} = \cos\vartheta\boldsymbol{I} + \sin\vartheta\boldsymbol{J}$.

and $\boldsymbol{u}_\mathrm{i} = [0, \omega_\mathrm{m}\psi_\mathrm{pm}]^\mathrm{T}$ is the voltage induced by the PM flux. This induced voltage can be considered as a load disturbance from the current controller point of view.

For the purposes of Section III, the stator voltage input in (2a) can be expressed in stator coordinates, leading to

$$\frac{\mathrm{d}\boldsymbol{\psi}_\mathrm{s}(t)}{\mathrm{d}t} = \boldsymbol{A}\boldsymbol{\psi}_\mathrm{s}(t) + \boldsymbol{B}'(t)\boldsymbol{u}_\mathrm{s}^\mathrm{s}(t) + \boldsymbol{b}\psi_\mathrm{pm} \tag{6}$$

where the time-varying input matrix is

$$\boldsymbol{B}'(t) = \mathrm{e}^{-\vartheta_\mathrm{m}(t)\boldsymbol{J}} \tag{7}$$

If constant ω_m is assumed, $\vartheta_\mathrm{m}(t) = \vartheta_\mathrm{m}(0) + \omega_\mathrm{m}t$ holds.

B. Preliminaries: Continuous-Time Current Control Design

For starters, a continuous-time 2DOF PI-type current controller is reviewed. A state controller with an integral action and reference feedforward will be used as a design framework. In the Laplace domain, this control law, expressed in rotor coordinates, is

$$\boldsymbol{u}_\mathrm{s,ref}(s) = \boldsymbol{K}_\mathrm{tc}\boldsymbol{i}_\mathrm{s,ref}(s) + \frac{\boldsymbol{K}_\mathrm{ic}}{s}[\boldsymbol{i}_\mathrm{s,ref}(s) - \boldsymbol{i}_\mathrm{s}(s)] - \boldsymbol{K}_\mathrm{1c}\boldsymbol{i}_\mathrm{s}(s) \tag{8}$$

where $\boldsymbol{u}_\mathrm{s,ref}$ is the resulting reference voltage, $\boldsymbol{i}_\mathrm{s,ref}$ is the reference current, $\boldsymbol{K}_\mathrm{tc}$ is the feedforward gain, $\boldsymbol{K}_\mathrm{ic}$ is the integral gain, and $\boldsymbol{K}_\mathrm{1c}$ is the state feedback gain. The gains are real 2×2 matrices. The voltage production of the inverter is assumed to be accurate and delayless, i.e., $\boldsymbol{u}_\mathrm{s} = \boldsymbol{u}_\mathrm{s,ref}$ holds. Using (4) and (8), the closed-loop current response becomes

$$\boldsymbol{i}_\mathrm{s}(s) = \boldsymbol{H}_\mathrm{c}(s)\boldsymbol{i}_\mathrm{s,ref}(s) - \boldsymbol{Y}_\mathrm{ic}(s)\boldsymbol{u}_\mathrm{i}(s) \tag{9}$$

The closed-loop transfer-function matrices for the reference following and disturbance rejection are

$$\boldsymbol{H}_\mathrm{c}(s) = (s^2\boldsymbol{I} + s\boldsymbol{A}_\mathrm{1c} + \boldsymbol{A}_\mathrm{0c})^{-1}(s\boldsymbol{B}_\mathrm{1c} + \boldsymbol{B}_\mathrm{0c}) \tag{10}$$

$$\boldsymbol{Y}_\mathrm{ic}(s) = (s^2\boldsymbol{I} + s\boldsymbol{A}_\mathrm{1c} + \boldsymbol{A}_\mathrm{0c})^{-1}(s\boldsymbol{C}) \tag{11}$$

where

$$\boldsymbol{A}_\mathrm{0c} = \boldsymbol{C}\boldsymbol{K}_\mathrm{ic}, \quad \boldsymbol{A}_\mathrm{1c} = \boldsymbol{C}(\boldsymbol{K}_\mathrm{1c} - \boldsymbol{A}\boldsymbol{C}^{-1})$$
$$\boldsymbol{B}_\mathrm{0c} = \boldsymbol{C}\boldsymbol{K}_\mathrm{ic}, \quad \boldsymbol{B}_\mathrm{1c} = \boldsymbol{C}\boldsymbol{K}_\mathrm{tc} \tag{12}$$

General control objectives for current controllers are: 1) no cross-coupling between the d- and q-axis and 2) the same closed-loop dynamics for both the axes. Hence, the non-diagonal elements of $\boldsymbol{H}_\mathrm{c}(s)$ should be zero due to the first objective and the diagonal elements should be equal due to the second objective. The resulting desired closed-loop transfer-function matrix is of the form

$$\boldsymbol{H}_{\mathrm{c}\star}(s) = \frac{b_\mathrm{1c}s + b_\mathrm{0c}}{s^2 + a_\mathrm{1c}s + a_\mathrm{0c}}\boldsymbol{I} \tag{13}$$

Based on (12) and (13), the closed-loop poles and zeros can be placed using the relations

$$\boldsymbol{K}_\mathrm{tc} = b_\mathrm{1c}\hat{\boldsymbol{C}}^{-1}, \quad \boldsymbol{K}_\mathrm{ic} = a_\mathrm{0c}\hat{\boldsymbol{C}}^{-1}$$
$$\boldsymbol{K}_\mathrm{1c} = \hat{\boldsymbol{A}}\hat{\boldsymbol{C}}^{-1} + a_\mathrm{1c}\hat{\boldsymbol{C}}^{-1} \tag{14}$$

where the hat indicates parameter estimates, e.g.:

$$\hat{\boldsymbol{C}}^{-1} = \begin{bmatrix} \hat{L}_\mathrm{d} & 0 \\ 0 & \hat{L}_\mathrm{q} \end{bmatrix} \tag{15}$$

Choosing the design parameters[2]

$$a_{0\mathrm{c}} = \alpha^2, \quad a_{1\mathrm{c}} = 2\alpha, \quad b_{1\mathrm{c}} = \alpha \tag{16}$$

the transfer-function matrix (13) reduces to the first-order unity-gain low-pass filter

$$\boldsymbol{H}_{\mathrm{c}\star}(s) = \frac{\alpha}{s+\alpha}\boldsymbol{I} \tag{17}$$

where α is the desired closed-loop control bandwidth. If accurate parameter estimates in (14) are assumed, $\boldsymbol{H}_\mathrm{c}(s) = \boldsymbol{H}_{\mathrm{c}\star}(s)$ holds. It can be easily shown that the controller corresponding to (8), (14), and (16) is equivalent to the 2DOF PI-type current controller considered in [2], [15], [16].

Advantages of this pole-placement design are its simplicity and easy tuning: only the desired bandwidth α and three parameter estimates ($\hat{R}_\mathrm{s}$, $\hat{L}_\mathrm{d}$, and $\hat{L}_\mathrm{q}$) are needed. For digital implementation, the algorithm has to be discretized using, e.g., the Euler or Tustin methods. Unfortunately, unless the sampling frequency is much higher than the closed-loop bandwidth and the maximum operating frequency, the actual closed-loop system deviates significantly from (17) due to discretization errors, leading to the cross-coupling between the d- and q-axis, oscillations, or even instability.

Assuming accurate parameter estimates in (14), the disturbance-rejection transfer-function matrix in (11) reduces to $\boldsymbol{Y}_{\mathrm{ic}\star}(s) = s/(s+\alpha)^2\boldsymbol{C}$. Alternatively, the poles and zeros could be placed using the complex vector design [3], which leads to the same desirable reference-following transfer-function matrix (17), but the disturbance-rejection transfer-function matrix becomes different. According to [3], the complex vector design reduces the sensitivity to parameter mismatch.

III. Discrete-Time Models

A. Exact Model

For the development of an exact discrete-time model, sampling of the stator currents is assumed to be synchronized with the pulse-width modulation (PWM). The switching-cycle averaged quantities are considered. Under these assumptions, the stator voltage in stator coordinates is piecewise constant between two consecutive sampling instants, which corresponds to the ZOH in stator coordinates. In other words, $\boldsymbol{u}_\mathrm{s}^\mathrm{s}(t)$ is constant during $kT_\mathrm{s} < t < (k+1)T_\mathrm{s}$, where T_s is the sampling period and k is the discrete-time index. The sampling frequency is defined by $f_\mathrm{s} = 1/T_\mathrm{s}$.

In the derivation of discrete-time models, two different approaches to model the stator-voltage input have been used in the literature depending on whether the ZOH of the voltage input is assumed to be in rotor coordinates [7], [17] or in stator coordinates [6], [8]. An additional compensation for the delay due to the ZOH is needed in the first approach [17]. The latter approach is chosen here, since it inherently takes the ZOH delay properly into account.

At this point, the system without the computational time delay is considered, i.e., only the effect of the ZOH in the stator-voltage input is taken into account. The system model will then be augmented with the time delay of one sampling period in Section III-D. When the stator flux is used as the state variable, the discrete-time state-space representation is given by

$$\boldsymbol{\psi}_\mathrm{s}(k+1) = \boldsymbol{\Phi}\boldsymbol{\psi}_\mathrm{s}(k) + \boldsymbol{\Gamma}\boldsymbol{u}_\mathrm{s}(k) + \boldsymbol{\gamma}\psi_\mathrm{pm} \tag{18a}$$

$$\boldsymbol{i}_\mathrm{s}(k) = \boldsymbol{C}\boldsymbol{\psi}_\mathrm{s}(k) + \boldsymbol{d}\psi_\mathrm{pm} \tag{18b}$$

where $\boldsymbol{\Phi}$, $\boldsymbol{\Gamma}$, $\boldsymbol{\gamma}$, $\boldsymbol{C}$, and $\boldsymbol{d}$ are the discrete-time system matrices. The discrete-time state matrix is

$$\boldsymbol{\Phi} = \mathrm{e}^{\boldsymbol{A}T_\mathrm{s}} = \begin{bmatrix} \phi_{11} & \phi_{12} \\ \phi_{21} & \phi_{22} \end{bmatrix} \tag{19}$$

The input matrix $\boldsymbol{B}'(t)$ in (7) corresponding to the stator voltage is time variant. Hence, the discrete-time input matrix becomes

$$\boldsymbol{\Gamma} = \int_0^{T_\mathrm{s}} \mathrm{e}^{\boldsymbol{A}\tau}\boldsymbol{B}'(T_\mathrm{s}-\tau)\mathrm{d}\tau \cdot \mathrm{e}^{\vartheta_\mathrm{m}(0)\boldsymbol{J}} = \begin{bmatrix} \gamma_{11} & \gamma_{12} \\ \gamma_{21} & \gamma_{22} \end{bmatrix} \tag{20}$$

The input matrix corresponding to the PM flux is

$$\boldsymbol{\gamma} = \int_0^{T_\mathrm{s}} \mathrm{e}^{\boldsymbol{A}\tau}\mathrm{d}\tau \cdot \boldsymbol{b} = \begin{bmatrix} \gamma_1 \\ \gamma_2 \end{bmatrix} \tag{21}$$

The closed-form expressions of the elements in (19)–(21) are given in the Appendix.

In the case of the SPMSM, where $L_\mathrm{d} = L_\mathrm{q} = L$, the exact discrete-time model becomes much simpler. As an example, the system matrices $\boldsymbol{\Phi}$ and $\boldsymbol{\Gamma}$ reduce to[3]

$$\boldsymbol{\Phi} = \mathrm{e}^{-\sigma T_\mathrm{s}}\mathrm{e}^{-\omega_\mathrm{m}T_\mathrm{s}\boldsymbol{J}}, \quad \boldsymbol{\Gamma} = \frac{1-\mathrm{e}^{-\sigma T_\mathrm{s}}}{\sigma}\mathrm{e}^{-\omega_\mathrm{m}T_\mathrm{s}\boldsymbol{J}} \tag{22}$$

where $\sigma = R_\mathrm{s}/L$. These expressions are mathematically identical to those given in [6], [8] (where the complex-valued space-vector notation has been used).

B. Approximation Based on Series Expansion

The system matrix $\boldsymbol{\Phi}$ in (18) can be expressed using the series expansion [18]

$$\boldsymbol{\Phi} = \boldsymbol{I} + T_\mathrm{s}\boldsymbol{A}\boldsymbol{\Psi} \tag{23}$$

where

$$\boldsymbol{\Psi} = \boldsymbol{I} + \frac{T_\mathrm{s}\boldsymbol{A}}{2!} + \frac{T_\mathrm{s}^2\boldsymbol{A}^2}{3!} + \ldots \tag{24}$$

The exact voltage input matrix $\boldsymbol{\Gamma}$ cannot be easily expressed as a series expansion due to the time-varying matrix $\boldsymbol{B}'(t)$ in (7). If the ZOH of the stator voltage were in rotor coordinates, the matrix $\boldsymbol{\Gamma}$ would equal $T_\mathrm{s}\boldsymbol{\Psi}\boldsymbol{B}$. However, the voltage is kept constant in stator coordinates during the sampling period as

[2]When placing the poles, it is often convenient to express the characteristic polynomial as $s^2 + 2\zeta\omega_0 s + \omega_0^2$, where ω_0 is undamped angular frequency and ζ is the damping ratio. Hence, $a_{0\mathrm{c}} = \omega_0^2$ and $a_{1\mathrm{c}} = 2\zeta\omega_0$.

[3]Unlike the IPMSM model, the SPMSM model could be expressed using complex space vectors by replacing the matrix $\boldsymbol{J}$ with the imaginary unit.

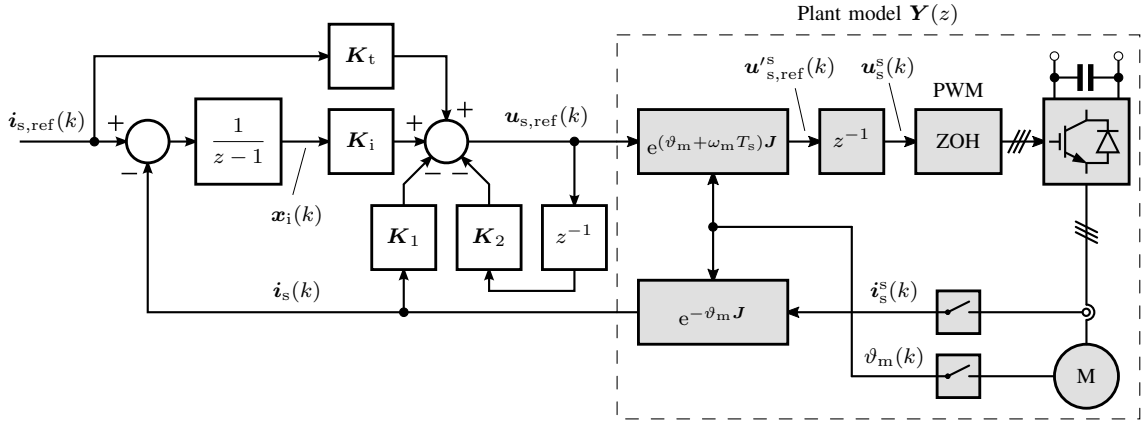

Fig. 1. 2DOF state-space current controller with an integral action. The sampling of the stator currents is synchronized with the PWM. The effects of the ZOH in stator coordinates, the coordinate transformations, and the computational time delay z^{-1} are included in the plant model. The angular error due to the time delay is compensated for in the coordinate transformation of the stator voltage. The gains $\boldsymbol{K}_1$, $\boldsymbol{K}_2$, $\boldsymbol{K}_{\mathrm{i}}$, and $\boldsymbol{K}_{\mathrm{t}}$ are 2×2 matrices.

discussed before. In [17], an approximate compensation for this effect was derived. Applying this compensation, the input matrix for the voltage can be approximated as

$$\boldsymbol{\Gamma} \approx T_{\mathrm{s}}\,\boldsymbol{\Psi}\boldsymbol{B}\frac{\omega_{\mathrm{m}}T_{\mathrm{s}}/2}{\sin(\omega_{\mathrm{m}}T_{\mathrm{s}}/2)}\mathrm{e}^{-(\omega_{\mathrm{m}}T_{\mathrm{s}}/2)\boldsymbol{J}} \tag{25}$$

Since the PM flux is constant in rotor coordinates, the input matrix for the PM flux is

$$\boldsymbol{\gamma} = T_{\mathrm{s}}\,\boldsymbol{\Psi}\boldsymbol{b} \tag{26}$$

Typically, only the first two terms of (24) are needed, i.e., $\boldsymbol{\Psi} = \boldsymbol{I} + (T_{\mathrm{s}}/2)\boldsymbol{A}$. Choosing $\boldsymbol{\Psi} = \boldsymbol{I}$ yields the Euler approximation, which suffices only at high sampling frequencies.

C. Current as a State Variable

The current control design becomes more straightforward, if the stator current is chosen as a state variable. With this selection, the state equation can be expressed as

$$\boldsymbol{i}_{\mathrm{s}}(k+1) = \boldsymbol{F}\boldsymbol{i}_{\mathrm{s}}(k) + \boldsymbol{G}\boldsymbol{u}_{\mathrm{s}}(k) + \boldsymbol{g}\psi_{\mathrm{pm}} \tag{27}$$

where the new system matrices are

$$\boldsymbol{F} = \boldsymbol{C}\boldsymbol{\Phi}\boldsymbol{C}^{-1}, \quad \boldsymbol{G} = \boldsymbol{C}\boldsymbol{\Gamma}, \quad \boldsymbol{g} = (\boldsymbol{I}-\boldsymbol{F})\boldsymbol{d} + \boldsymbol{C}\boldsymbol{\gamma} \tag{28}$$

D. Inclusion of the Control Delay

Fig. 1 shows the plant model from the control system point of view. As shown in the figure, the digital control system and PWM update have (at least) one-sampling-period time delay due to the finite computation time, i.e., $\boldsymbol{u}^{\mathrm{s}}_{\mathrm{s}}(k) = \boldsymbol{u}'^{\mathrm{s}}_{\mathrm{s,ref}}(k-1)$ in stator coordinates, or, when transformed into rotor coordinates, $\boldsymbol{u}_{\mathrm{s}}(k) = \mathrm{e}^{-\omega_{\mathrm{m}}T_{\mathrm{s}}\boldsymbol{J}}\boldsymbol{u}'_{\mathrm{s,ref}}(k-1)$. To simplify the notation, $\boldsymbol{u}_{\mathrm{s,ref}} = \mathrm{e}^{-\omega_{\mathrm{m}}T_{\mathrm{s}}\boldsymbol{J}}\boldsymbol{u}'_{\mathrm{s,ref}}$ is defined, giving $\boldsymbol{u}_{\mathrm{s}}(k) = \boldsymbol{u}_{\mathrm{s,ref}}(k-1)$. The effect of the time delay on the voltage angle can be easily compensated for in the coordinate transformation of the reference voltage (cf. Fig. 1).

For control design, the time delay can be included in the plant model as [18]

$$\begin{bmatrix}\boldsymbol{i}_{\mathrm{s}}(k+1)\\ \boldsymbol{u}_{\mathrm{s}}(k+1)\end{bmatrix} = \begin{bmatrix}\boldsymbol{F} & \boldsymbol{G}\\ \boldsymbol{O} & \boldsymbol{O}\end{bmatrix}\begin{bmatrix}\boldsymbol{i}_{\mathrm{s}}(k)\\ \boldsymbol{u}_{\mathrm{s}}(k)\end{bmatrix} + \begin{bmatrix}\boldsymbol{O}\\ \boldsymbol{I}\end{bmatrix}\boldsymbol{u}_{\mathrm{s,ref}}(k) + \begin{bmatrix}\boldsymbol{g}\\ \boldsymbol{0}\end{bmatrix}\psi_{\mathrm{pm}} \tag{29}$$

It is worth noticing that both the states are readily available as feedback signals in the state feedback control: $\boldsymbol{i}_{\mathrm{s}}$ is the measured feedback and $\boldsymbol{u}_{\mathrm{s}}$ is obtained from the previous value of the reference voltage $\boldsymbol{u}_{\mathrm{s,ref}}$.

In the following section, the current controller will be designed based on the reference-following dynamics (similarly as in Section II-B). The effect of the disturbance voltage $\boldsymbol{u}_{\mathrm{i}}$ on the stator current will be omitted for simplicity. If needed, its effect can be analyzed separately based on the superposition principle. Hence, from (29), the stator current in the z-domain can be expressed as $\boldsymbol{i}_{\mathrm{s}}(z) = \boldsymbol{Y}(z)\boldsymbol{u}_{\mathrm{s,ref}}(z)$, where

$$\boldsymbol{Y}(z) = z^{-1}(z\boldsymbol{I} - \boldsymbol{F})^{-1}\boldsymbol{G} \tag{30}$$

IV. Discrete-Time Current Control Design

A. Framework

A 2DOF state-space controller with an integral action, shown in Fig. 1, is considered. The control law is

$$\boldsymbol{x}_{\mathrm{i}}(k+1) = \boldsymbol{x}_{\mathrm{i}}(k) + \boldsymbol{i}_{\mathrm{s,ref}}(k) - \boldsymbol{i}_{\mathrm{s}}(k) \tag{31a}$$

$$\begin{aligned}\boldsymbol{u}_{\mathrm{s,ref}}(k) = {}& \boldsymbol{K}_{\mathrm{t}}\boldsymbol{i}_{\mathrm{s,ref}}(k) + \boldsymbol{K}_{\mathrm{i}}\boldsymbol{x}_{\mathrm{i}}(k)\\ & - \boldsymbol{K}_1\boldsymbol{i}_{\mathrm{s}}(k) - \boldsymbol{K}_2\boldsymbol{u}_{\mathrm{s}}(k)\end{aligned} \tag{31b}$$

where $\boldsymbol{x}_{\mathrm{i}}$ is the integral state, $\boldsymbol{K}_{\mathrm{i}}$ is the integral gain, $\boldsymbol{K}_{\mathrm{t}}$ is the feedforward gain, $\boldsymbol{K}_1$ and $\boldsymbol{K}_2$ are the state-feedback gains, and $\boldsymbol{u}_{\mathrm{s}}(k+1) = \boldsymbol{u}_{\mathrm{s,ref}}(k)$. Since all the states are directly available, the closed-loop poles can be placed arbitrarily. The control law (31) can be expressed in the z-domain as

$$\begin{aligned}\boldsymbol{u}_{\mathrm{s,ref}}(z) = {}& \boldsymbol{K}_{\mathrm{t}}\boldsymbol{i}_{\mathrm{s,ref}}(z) + \frac{\boldsymbol{K}_{\mathrm{i}}}{z-1}[\boldsymbol{i}_{\mathrm{s,ref}}(z) - \boldsymbol{i}_{\mathrm{s}}(z)]\\ & - \boldsymbol{K}_1\boldsymbol{i}_{\mathrm{s}}(z) - \frac{\boldsymbol{K}_2}{z}\boldsymbol{u}_{\mathrm{s,ref}}(z)\end{aligned} \tag{32}$$

From (30) and (32), the closed-loop dynamics become

$$\boldsymbol{i}_{\mathrm{s}}(z) = \boldsymbol{H}(z)\boldsymbol{i}_{\mathrm{s,ref}}(z) \tag{33}$$

where

$$\boldsymbol{H}(z) = (z^3\boldsymbol{I} + z^2\boldsymbol{A}_2 + z\boldsymbol{A}_1 + \boldsymbol{A}_0)^{-1}(z\boldsymbol{B}_1 + \boldsymbol{B}_0) \tag{34}$$

and the matrices are

$$\begin{aligned}\boldsymbol{A}_0 &= \boldsymbol{G}(\boldsymbol{K}_2\boldsymbol{G}^{-1}\boldsymbol{F} + \boldsymbol{K}_\mathrm{i} - \boldsymbol{K}_1)\\ \boldsymbol{A}_1 &= \boldsymbol{F} + \boldsymbol{G}[\boldsymbol{K}_1 - \boldsymbol{K}_2\boldsymbol{G}^{-1}(\boldsymbol{I} + \boldsymbol{F})]\\ \boldsymbol{A}_2 &= \boldsymbol{G}\boldsymbol{K}_2\boldsymbol{G}^{-1} - \boldsymbol{I} - \boldsymbol{F}\\ \boldsymbol{B}_0 &= \boldsymbol{G}(\boldsymbol{K}_\mathrm{i} - \boldsymbol{K}_\mathrm{t}), \quad \boldsymbol{B}_1 = \boldsymbol{G}\boldsymbol{K}_\mathrm{t}\end{aligned} \tag{35}$$

A closed-loop state-space representation can be formed from (29) and (31) as

$$\begin{bmatrix}\boldsymbol{i}_\mathrm{s}(k+1)\\ \boldsymbol{u}_\mathrm{s}(k+1)\\ \boldsymbol{x}_\mathrm{i}(k+1)\end{bmatrix} = \begin{bmatrix}\boldsymbol{F} & \boldsymbol{G} & \boldsymbol{O}\\ -\boldsymbol{K}_1 & -\boldsymbol{K}_2 & \boldsymbol{K}_\mathrm{i}\\ -\boldsymbol{I} & \boldsymbol{O} & \boldsymbol{I}\end{bmatrix}\begin{bmatrix}\boldsymbol{i}_\mathrm{s}(k)\\ \boldsymbol{u}_\mathrm{s}(k)\\ \boldsymbol{x}_\mathrm{i}(k)\end{bmatrix} \tag{36}$$

where the inputs are omitted for simplicity. The poles of (34) equal the eigenvalues of the system matrix in (36). The system is stable if the eigenvalues are inside the unit circle. When analyzing the robustness of the system, it is worth noticing that $\boldsymbol{F}$ and $\boldsymbol{G}$ should be the exact system matrices calculated using the actual motor parameters, while the gains can be based on approximations and erroneous parameter estimates (depending on the controller under analysis). If the control design is based on the exact model and the motor parameters are perfectly known, the eigenvalues of (36) equal the desired closed-loop poles.

B. Approximation of the Continuous-Time Design

The gains of the discrete-time controller (31) can be determined by approximating the continuous-time controller (cf. Section II-B) with the Euler method. In the framework of Fig. 1, the angular error of $\omega_\mathrm{m}T_\mathrm{s}$ due to the computational delay is compensated for in the coordinate transformation. When approximating continuous-time designs, the angular error of $\omega_\mathrm{m}T_\mathrm{s}/2$ caused by the ZOH delay should also be taken into account [17]. Embedding this compensation into the gains yields

$$\begin{aligned}\boldsymbol{K}_1 &= \mathrm{e}^{(\omega_\mathrm{m}T_\mathrm{s}/2)\boldsymbol{J}}\left(2\alpha\hat{\boldsymbol{C}}^{-1} - \hat{R}_\mathrm{s}\boldsymbol{I} - \omega_\mathrm{m}\boldsymbol{J}\hat{\boldsymbol{C}}^{-1}\right), \quad \boldsymbol{K}_2 = \boldsymbol{O}\\ \boldsymbol{K}_\mathrm{t} &= \mathrm{e}^{(\omega_\mathrm{m}T_\mathrm{s}/2)\boldsymbol{J}}\alpha\hat{\boldsymbol{C}}^{-1}, \quad \boldsymbol{K}_\mathrm{i} = \mathrm{e}^{(\omega_\mathrm{m}T_\mathrm{s}/2)\boldsymbol{J}}T_\mathrm{s}\alpha^2\hat{\boldsymbol{C}}^{-1}\end{aligned} \tag{37}$$

The performance of this design is acceptable if the sampling frequency is about twenty times higher than the closed-loop bandwidth and the operating frequency. At lower sampling frequencies, direct discrete-time design methods are preferred.

C. Proposed Direct Discrete-Time Design

General control objectives for current controllers in the case of the discrete-time design are the same as in the continuous-time case, cf. Section II-B. Hence, the non-diagonal elements of $\boldsymbol{H}(z)$ in (34) should be zero in order to avoid cross-coupling of the axes and the diagonal elements should be equal in order to achieve the same dynamics for both the axes. The desirable closed-loop transfer-function matrix is of the form

$$\boldsymbol{H}_\star(z) = \frac{b_1 z + b_0}{z^3 + a_2 z^2 + a_1 z + a_0}\boldsymbol{I} \tag{38}$$

Due to the time delay, $a_0 = 0$ is selected. The gain matrices can be solved using (35) and (38):

$$\begin{aligned}\boldsymbol{K}_1 &= \boldsymbol{K}_\mathrm{i} + (1+a_2)\hat{\boldsymbol{G}}^{-1}\hat{\boldsymbol{F}} + \hat{\boldsymbol{G}}^{-1}\hat{\boldsymbol{F}}^2\\ \boldsymbol{K}_2 &= (1+a_2)\boldsymbol{I} + \hat{\boldsymbol{G}}^{-1}\hat{\boldsymbol{F}}\hat{\boldsymbol{G}}\\ \boldsymbol{K}_\mathrm{t} &= b_1\hat{\boldsymbol{G}}^{-1}, \quad \boldsymbol{K}_\mathrm{i} = (1+a_1+a_2)\hat{\boldsymbol{G}}^{-1}\end{aligned} \tag{39}$$

Using these expressions, the poles and zero in (38) can be arbitrarily placed. The gains depend on the rotor speed via the matrices $\hat{\boldsymbol{F}}$ and $\hat{\boldsymbol{G}}$.

Choosing the coefficients $a_1 = \beta^2$, $a_2 = -2\beta$, and $b_1 = 1 - \beta$ leads to

$$\boldsymbol{H}_\star(z) = \frac{1-\beta}{z(z-\beta)}\boldsymbol{I} \tag{40}$$

where $\beta = \mathrm{e}^{-\alpha T_\mathrm{s}}$ is the exact mapping in the discrete domain of the intended real pole of the system. The diagonal matrix consists of the delay and the first-order unity-gain low-pass filter; the pole in (38) is cancelled by the zero in a similar manner as in the continuous-time case in (17), cf. Section II-B. In digital control, the computational time delay z^{-1} cannot be avoided in practice. It is worth noticing that the same input parameters for the design are needed as in the continuous-time case ($\hat{R}_\mathrm{s}$, $\hat{L}_\mathrm{d}$, $\hat{L}_\mathrm{q}$, and α). The proposed design can be seen as a discrete-time counterpart to the control law presented in Section II-B.

V. Results

A transverse-laminated 6.7-kW four-pole SyRM is considered. The rated values of the motor are: speed 3175 r/min; frequency 105.8 Hz; line-to-line rms voltage 370 V; and rms current 15.5 A. Four different current control designs have been evaluated:

- Design 1: approximation of the continuous-time design;
- Design 2: proposed design based on the approximate model with $\boldsymbol{\Psi} = \boldsymbol{I}$;
- Design 3: proposed design based on the approximate model with $\boldsymbol{\Psi} = \boldsymbol{I} + (T_\mathrm{s}/2)\boldsymbol{A}$;
- Design 4: proposed design based on the exact model.

For brevity, only selected results are presented in the following.

A. Robustness Analysis

The robustness of the four current control designs against parameter errors is analyzed by calculating the eigenvalues of (36). The controller gains have been calculated using the parameter estimates $\hat{L}_\mathrm{d} = 2.0$ p.u., $\hat{L}_\mathrm{q} = 0.3$ p.u., and $\hat{R}_\mathrm{s} = 0.04$ p.u. The desired bandwidth α is varied in a range from 0 to $2\pi{\cdot}500$ rad/s.

Fig. 2 shows the stability maps as a function of the desired bandwidth α and the ratio $L_\mathrm{q}/\hat{L}_\mathrm{q}$. The actual inductance L_q is varied in a range from 0 to $2.5\hat{L}_\mathrm{q}$, while other actual parameters perfectly match with their estimates. Figs. 2(a) and 2(b) show the stability maps at zero speed when the sampling frequency is 2 kHz and 1 kHz, respectively. It can be seen that Design 1 has clearly the smallest stable regions: the

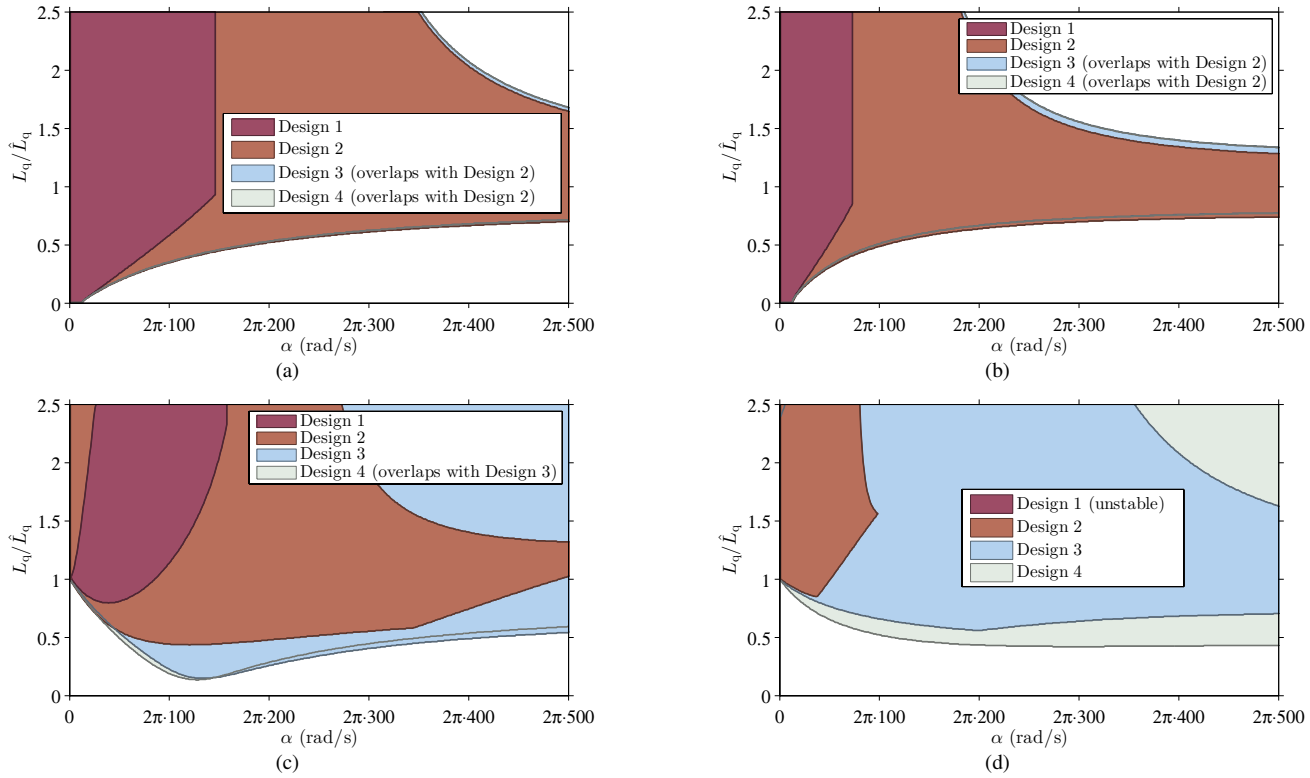

Fig. 2. Stability maps for the four different current control designs as a function of the desired bandwidth α and the ratio $L_\mathrm{q}/\hat{L}_\mathrm{q}$: (a) electrical angular speed $\omega_\mathrm{m} = 0$ of the rotor, the sampling frequency $f_\mathrm{s} = 2$ kHz; (b) $\omega_\mathrm{m} = 0$, $f_\mathrm{s} = 1$ kHz; (c) $\omega_\mathrm{m} = 2\pi \cdot 200$ rad/s, $f_\mathrm{s} = 2$ kHz; and (d) $\omega_\mathrm{m} = 2\pi \cdot 200$ rad/s, $f_\mathrm{s} = 1$ kHz.

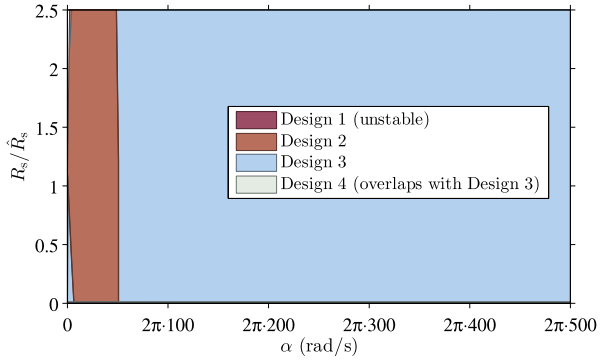

Fig. 3. Stability maps for the four different current control designs as a function of the desired bandwidth α and the ratio $R_\mathrm{s}/\hat{R}_\mathrm{s}$. The speed is $\omega_\mathrm{m} = 2\pi \cdot 200$ rad/s and the sampling frequency is $f_\mathrm{s} = 1$ kHz.

desired bandwidth α is limited to about $2\pi{\cdot}150$ rad/s when the sampling frequency is 2 kHz and to about $2\pi{\cdot}75$ rad/s when the sampling frequency is 1 kHz. The stable regions of Designs 3 and 4 basically overlap with those of Design 2, i.e., there are no significant differences between Designs 2…4. A comparison of Figs. 2(a) and 2(b) shows that decreasing the sampling frequency from 2 kHz to 1 kHz makes the stable regions smaller in all the designs. It is worth noticing that, if $L_\mathrm{q} > \hat{L}_\mathrm{q}$, the actual bandwidth becomes generally lower than the desired bandwidth α.

Figs. 2(c) and 2(d) show the stability maps at the electrical angular speed $\omega_\mathrm{m} = 2\pi \cdot 200$ rad/s when the sampling frequency is 2 kHz and 1 kHz, respectively. When the sampling frequency is 1 kHz, Design 1 has no stable region at all. Further, the stable region of Design 2 is very small: α is limited to about $2\pi{\cdot}50$ rad/s, if there are no parameter errors. The stable regions of Designs 3 and 4 are comparatively large. A comparison of Figs. 2(c) and 2(d) show that decreasing the sampling frequency from 2 kHz to 1 kHz makes the stable regions smaller in all the designs and the difference between Designs 3 and 4 increases.

The robustness against erroneous $\hat{L}_\mathrm{d}$ and $\hat{R}_\mathrm{s}$ has also been analyzed. In the case of $\hat{L}_\mathrm{d}$, the results are very similar to those in Fig. 2 and are not shown here. All the current control designs are almost insensitive to errors in $\hat{R}_\mathrm{s}$ in the whole speed range. As an example, Fig. 3 shows the stability maps as a function of the desired bandwidth α and the ratio $R_\mathrm{s}/\hat{R}_\mathrm{s}$. The actual resistance R_s is varied in a range from 0 to $2.5\hat{R}_\mathrm{s}$, while other actual parameters perfectly match with their estimates. The speed is $\omega_\mathrm{m} = 2\pi \cdot 200$ rad/s and the sampling frequency is 1 kHz. It can be seen that the stable region of Design 2 is almost independent of the stator resistance error. Further, the stable regions of Designs 3 and 4 effectively cover the whole area. Design 1 is unstable due to the low sampling frequency (independently of the stator resistance error).

It is worth noticing that the actual parameters were assumed to be constant (but erroneous) in this robustness analysis. In practice, the actual inductances may vary significantly (due to the magnetic saturation) even during one sampling period,

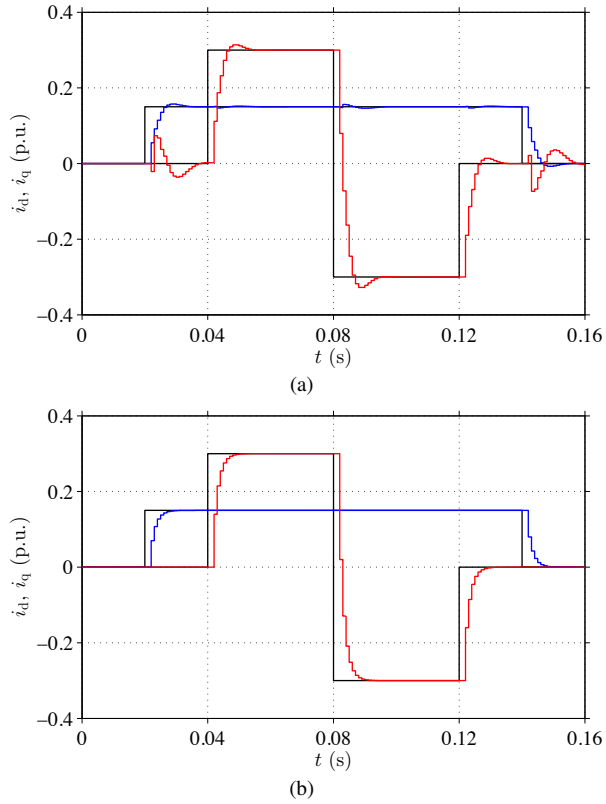

Fig. 4. Simulation results at the speed $\omega_\mathrm{m} = 2\pi \cdot 200$ rad/s with the accurate parameter estimates: (a) Design 3; (b) Design 4. The desired bandwidth is $\alpha = 2\pi \cdot 100$ rad/s and the sampling frequency is $f_\mathrm{s} = 1$ kHz. Sampled values of i_d (blue), i_q (red), and their references (black) are shown.

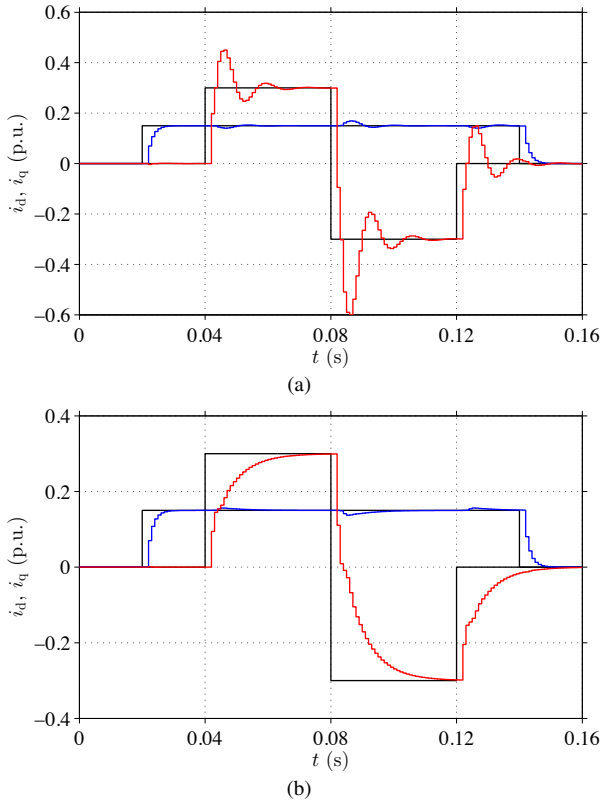

Fig. 5. Simulation results at the speed $\omega_\mathrm{m} = 2\pi \cdot 200$ rad/s for Design 4: (a) $L_\mathrm{q} = 0.7\hat{L}_\mathrm{q}$; (b) $L_\mathrm{q} = 1.5\hat{L}_\mathrm{q}$. The desired bandwidth is $\alpha = 2\pi \cdot 100$ rad/s and the sampling frequency is $f_\mathrm{s} = 1$ kHz. Sampled values of i_d (blue), i_q (red), and their references (black) are shown.

which causes additional bandwidth limitations.

B. Simulation Results

Figs. 4 and 5 show time-domain simulation results of the current waveforms. The electrical angular speed of the rotor is $\omega_\mathrm{m} = 2\pi \cdot 200$ rad/s. The desired bandwidth is $\alpha = 2\pi \cdot 100$ rad/s and the sampling frequency is 1 kHz. The current references $i_\mathrm{d,ref}$ and $i_\mathrm{q,ref}$ are changed stepwise. The sampled values of the current components i_d and i_q are shown (but the ripple between the sampling instants is fairly large at this low sampling frequencies, cf. [7]).

Figs. 4(a) and 4(b) show the results for Designs 3 and 4, respectively. The actual parameters perfectly match with their estimates. Some cross-coupling and overshoot appears in Fig. 4(a), while the results in Fig. 4(b) completely agree with the desired performance. If the sampling frequency were increased to 2 kHz, the results of Design 3 would become very close to those of Design 4. In accordance with the stability maps in Fig. 2(d), the time-domain simulations for Designs 1 and 2 were unstable under these operating conditions.

Fig. 5 demonstrates the effects of parameter mismatches on the step responses in the case of Design 4. The actual inductance is $L_\mathrm{q} = 0.7\hat{L}_\mathrm{q}$ in Fig. 5(a), where significant oscillations appear. These oscillations could also be anticipated based on Fig. 2(d), where the given operating condition is close to the stability boundary. In Fig. 5(b), the actual inductance is $L_\mathrm{q} = 1.5\hat{L}_\mathrm{q}$. The step response is now well damped, but the actual bandwidth is much less than the desired bandwidth.

C. Experimental Results

The discrete-time current controllers were experimentally investigated using the 6.7-kW SyRM drive. A servo induction machine was used as a loading machine in the speed-control mode. The four current control designs (described in the beginning of the section) were implemented in a dSPACE DS1104 PPC/DSP board. The sampling was synchronized with the PWM. The sampling and switching frequencies were 2 kHz.

The actual inductances $L_\mathrm{d}(i_\mathrm{d}, i_\mathrm{q})$ and $L_\mathrm{q}(i_\mathrm{d}, i_\mathrm{q})$ of the SyRM depend significantly on the current components due to the magnetic saturation. The saturation effects were modeled in the estimates $\hat{L}_\mathrm{d}$ and $\hat{L}_\mathrm{q}$ by means of the power functions [19]. In order to properly model the effect of the differential inductances, a one-step prediction of the inductance estimates would be needed, since the transformations in (28) become $\boldsymbol{F}(k) = \boldsymbol{C}(k+1)\boldsymbol{\Phi}(k)\boldsymbol{C}^{-1}(k)$ and $\boldsymbol{G}(k) = \boldsymbol{C}(k+1)\boldsymbol{\Gamma}(k)$. Here, for simplicity, the effect of the differential inductances was omitted, i.e., the matrices were calculated as $\hat{\boldsymbol{F}}(k) = \hat{\boldsymbol{C}}(k)\hat{\boldsymbol{\Phi}}(k)\hat{\boldsymbol{C}}^{-1}(k)$ and $\hat{\boldsymbol{G}}(k) = \hat{\boldsymbol{C}}(k)\hat{\boldsymbol{\Gamma}}(k)$.

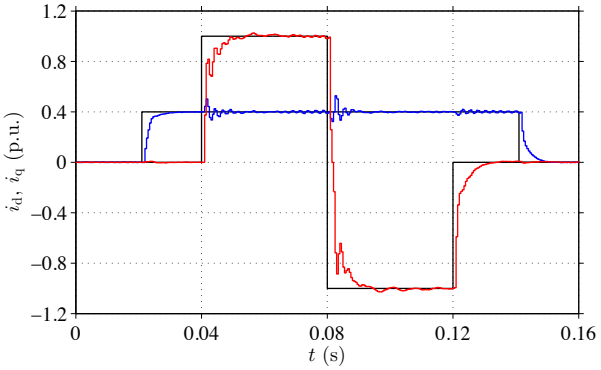

Fig. 6. Experimental results at the rotor speed $\omega_\mathrm{m} = 0$ for Design 4. The desired bandwidth is $\alpha = 2\pi \cdot 100$ rad/s and the sampling frequency is $f_\mathrm{s} = 2$ kHz. Sampled values of i_d (blue), i_q (red), and their references (black) are shown.

Fig. 6 shows an example of experimental results at zero speed. The current references are changed stepwise. Design 4 is used. Designs 2 and 3 gave similar results, in accordance with the stability maps in Fig. 2(a). It can be seen that the control response is close to the desired response, except for the oscillations after the steps in $i_{\mathrm{q,ref}}$. The fast change in i_q causes both L_d and L_q change substantially even during one sampling period. The cross-saturation also causes some cross-coupling between the d- and q-axis. These oscillations could probably be reduced by taking the effect of the differential inductances into account in the saturation model. Generally, the saturation effects tend to be less severe in IPMSMs and PM-assisted SyRMs than in SyRMs.

Fig. 7 shows examples of experimental results at the rotor speed $\omega_\mathrm{m} = 2\pi \cdot 200$ rad/s. The desired bandwidth is $\alpha = 2\pi \cdot 100$ rad/s and the sampling frequency is 2 kHz. Designs 2 and 4 are used in Figs. 7(a) and 7(b), respectively. The stator voltage is approximately zero until $t = 0.02$ s, but after the step in $i_{\mathrm{d,ref}}$, the voltage increases up to about 80% of the rated value. The system remains stable in the case of Design 2, but much noise and some cross-coupling can be observed. The performance of Design 4 is much better. The ripple seen in the waveforms in Fig. 7(b) originates mainly from the imperfect magnetic saturation model. At this sampling frequency of 2 kHz, the results for Design 3 were very similar to those for Design 4 shown in Fig. 7(b), in accordance with the stability maps in Fig. 2(c).

VI. Conclusions

An exact closed-form hold-equivalent discrete model of IPMSM and SyRM drives was derived. The model can be applied to design, analysis, and implementation of controllers and observers. Further, an analytical discrete pole-placement design method for a 2DOF state-space current controller with an integral action was proposed. The time delays are inherently taken into account in the design. The proposed design method is easy to apply: only the desired closed-loop bandwidth and three motor parameters are needed. The hold-equivalent model applied in the current control design can be either the exact

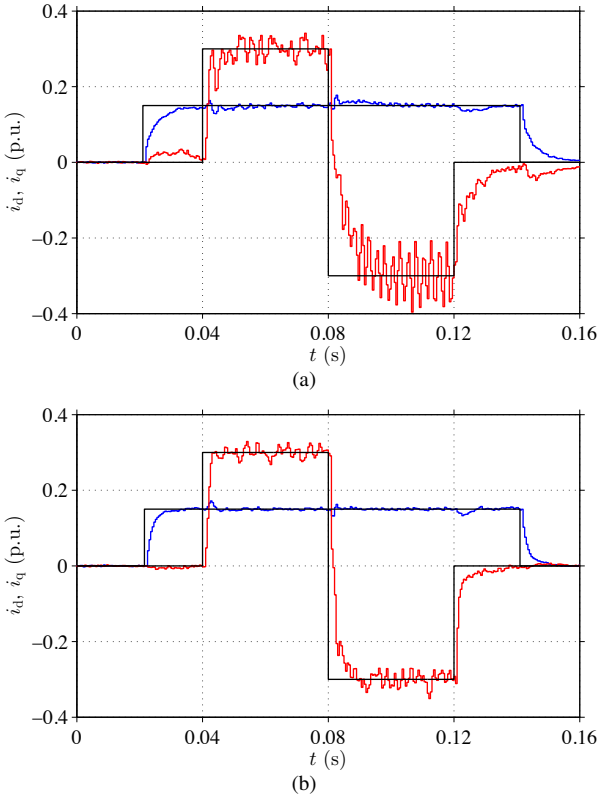

Fig. 7. Experimental results at the rotor speed $\omega_\mathrm{m} = 2\pi \cdot 200$ rad/s: (a) Design 2; (b) Design 4. The desired bandwidth is $\alpha = 2\pi \cdot 100$ rad/s and the sampling frequency is $f_\mathrm{s} = 2$ kHz. Sampled values of i_d (blue), i_q (red), and their references (black) are shown.

model or a series expansion (where one more term than in the Euler method already gives good results). According to the results of eigenvalue analysis, simulations, and experiments, the proposed design improves the dynamic performance and robustness especially at high speeds as compared to the benchmark methods. The design method is directly applicable to SPMSM drives as well.

Appendix
Exact Discrete-Time Model

The closed-form solutions for the elements of $\boldsymbol{\Phi}$ in (19) are

$$\begin{aligned}
\phi_{11} &= \mathrm{e}^{-\sigma T_\mathrm{s}} \left[\cosh(\lambda T_\mathrm{s}) - \delta \frac{\sinh(\lambda T_\mathrm{s})}{\lambda} \right] \\
\phi_{22} &= \mathrm{e}^{-\sigma T_\mathrm{s}} \left[\cosh(\lambda T_\mathrm{s}) + \delta \frac{\sinh(\lambda T_\mathrm{s})}{\lambda} \right] \\
\phi_{21} &= -\phi_{12} = -\omega_\mathrm{m} \mathrm{e}^{-\sigma T_\mathrm{s}} \frac{\sinh(\lambda T_\mathrm{s})}{\lambda}
\end{aligned} \tag{41}$$

where $\lambda = \sqrt{\delta^2 - \omega_\mathrm{m}^2}$ and[4]

$$\sigma = \frac{R_\mathrm{s}}{2} \left(\frac{1}{L_\mathrm{d}} + \frac{1}{L_\mathrm{q}} \right), \quad \delta = \frac{R_\mathrm{s}}{2} \left(\frac{1}{L_\mathrm{d}} - \frac{1}{L_\mathrm{q}} \right) \tag{42}$$

[4]If $\omega_\mathrm{m}^2 > \delta^2$, then $\lambda = \mathrm{j}\lambda_\mathrm{im} = \mathrm{j}\sqrt{\omega_\mathrm{m}^2 - \delta^2}$ is imaginary. All the matrix elements remain real since $\cosh(\mathrm{j}\lambda_\mathrm{im} T_\mathrm{s}) = \cos(\lambda_\mathrm{im} T_\mathrm{s})$ and $\sinh(\mathrm{j}\lambda_\mathrm{im} T_\mathrm{s})/(\mathrm{j}\lambda_\mathrm{im}) = \sin(\lambda_\mathrm{im} T_\mathrm{s})/\lambda_\mathrm{im}$ hold due to the properties of hyperbolic functions. Furthermore, for $\lambda = 0$, these functions reduce to $\cosh(\lambda T_\mathrm{s}) = \sinh(\lambda T_\mathrm{s})/\lambda = 1$.

The closed-form solutions for the elements of $\boldsymbol{\Gamma}$ in (20) are

$$\begin{aligned}
\gamma_{11} &= G\Big[g_{11}\cos(\omega_\mathrm{m}T_\mathrm{s}) - g_{12}\sin(\omega_\mathrm{m}T_\mathrm{s}) - g_{11}\phi_{11} \\
&\qquad + (\sigma+\delta)\omega_\mathrm{m}^2(\phi_{11}-\phi_{22})\Big] \\
\gamma_{12} &= G\Big[g_{12}\cos(\omega_\mathrm{m}T_\mathrm{s}) + g_{11}\sin(\omega_\mathrm{m}T_\mathrm{s}) - g_{12}\phi_{11} + g_{22}\phi_{21}\Big] \\
\gamma_{21} &= G\Big[g_{21}\cos(\omega_\mathrm{m}T_\mathrm{s}) - g_{22}\sin(\omega_\mathrm{m}T_\mathrm{s}) - g_{21}\phi_{22} - g_{11}\phi_{21}\Big] \\
\gamma_{22} &= G\Big[g_{22}\cos(\omega_\mathrm{m}T_\mathrm{s}) + g_{21}\sin(\omega_\mathrm{m}T_\mathrm{s}) - g_{22}\phi_{22} \\
&\qquad + (\sigma-\delta)\omega_\mathrm{m}^2(\phi_{22}-\phi_{11})\Big]
\end{aligned} \tag{43}$$

where $G = 1/[(\sigma^2-\delta^2)^2 + 4\sigma^2\omega_\mathrm{m}^2]$ and

$$\begin{aligned}
g_{11} &= (\sigma-\delta)^2(\sigma+\delta) + 4\sigma\omega_\mathrm{m}^2, \quad g_{12} = 2(\sigma-\delta)\delta\omega_\mathrm{m} \\
g_{21} &= 2(\sigma+\delta)\delta\omega_\mathrm{m}, \quad g_{22} = (\sigma+\delta)^2(\sigma-\delta) + 4\sigma\omega_\mathrm{m}^2
\end{aligned} \tag{44}$$

In the previous derivations, it is important to notice that $\mathrm{e}^{x+y} = \mathrm{e}^x\mathrm{e}^y$ does not hold for matrix exponentials in general. The elements of $\boldsymbol{\gamma}$ in (21) are given by

$$\begin{aligned}
\gamma_1 &= H\left[(\sigma-\delta)(1-\phi_{11}) - \omega_\mathrm{m}\phi_{21}\right] \\
\gamma_2 &= H\left[-\sigma\phi_{21} + \omega_\mathrm{m}\left(\frac{\phi_{11}+\phi_{22}}{2} - 1\right)\right]
\end{aligned} \tag{45}$$

where $H = (\sigma+\delta)/[(\sigma+\delta)(\sigma-\delta) + \omega_\mathrm{m}^2]$.

ACKNOWLEDGMENT

The authors would like to thank Mr. Daniel Koslopp for preliminary analyses of discrete models. The work was supported in part by ABB Oy and in part by the Academy of Finland.

REFERENCES

[1] T. M. Rowan and R. J. Kerkman, "A new synchronous current regulator and an analysis of current-regulated PWM inverters," *IEEE Trans. Ind. Appl.*, vol. IA-22, no. 4, pp. 678–690, July/Aug. 1986.

[2] L. Harnefors and H.-P. Nee, "Model-based current control of AC machines using the internal model control method," *IEEE Trans. Ind. Appl.*, vol. 34, no. 1, pp. 133–141, Jan./Feb. 1998.

[3] F. Briz del Blanco, M. W. Degner, and R. D. Lorenz, "Dynamic analysis of current regulators for AC motors using complex vectors," *IEEE Trans. Ind. Appl.*, vol. 35, no. 6, pp. 1424–1432, Nov./Dec. 1999.

[4] F. Briz, M. W. Degner, and R. D. Lorenz, "Analysis and design of current regulators using complex vectors," *IEEE Trans. Ind. Appl.*, vol. 36, no. 3, pp. 817–825, May/June 2000.

[5] H. Kim and R. D. Lorenz, "Improved current regulators for IPM machine drives using on-line parameter estimation," in *Conf. Rec. IEEE-IAS Annu. Meeting*, vol. 1, Pittsburgh, PA, Oct. 2002, pp. 86–91.

[6] K.-K. Huh and R. D. Lorenz, "Discrete-time domain modeling and design for AC machine current regulation," in *Conf. Rec. IEEE-IAS Annu. Meeting*, New Orleans, LA, Sept. 2007, pp. 2066–2073.

[7] J.-S. Yim, S.-K. Sul, B.-H. Bae, N. R. Patel, and S. Hiti, "Modified current control schemes for high-performance permanent-magnet AC drives with low sampling to operating frequency ratio," *IEEE Trans. Ind. Appl.*, vol. 45, no. 2, pp. 763–771, Mar./Apr. 2009.

[8] H. Kim, M. W. Degner, J. M. Guerrero, F. Briz, and R. D. Lorenz, "Discrete-time current regulator design for AC machine drives," *IEEE Trans. Ind. Appl.*, vol. 46, no. 4, pp. 1425–1435, July/Aug. 2010.

[9] W. Peters, T. Huber, and J. Böcker, "Control realization for an interior permanent magnet synchronous motor (IPMSM) in automotive drive trains," in *Conf. PCIM 2011*, vol. 1, Nuremberg, Germany, May 2011, pp. 98–103.

[10] W. Peters and J. Böcker, "Discrete-time design of adaptive current controller for interior permanent magnet synchronous motors (IPMSM) with high magnetic saturation," in *Proc. IEEE IECON'13*, Vienna, Austria, Nov. 2013, pp. 6608–6613.

[11] A. Altomare, A. Guagnano, F. Cupertino, and D. Naso, "Discrete-time control of high speed salient machines," in *Proc. IEEE ECCE 2014*, Pittsburgh, PA, Sept. 2014, pp. 3528–3534.

[12] J.-C. Alacoque, "Discrete-time modelling — flux and torque deadbeat control for induction machine," in *Proc. EPE-PEMC'06*, Portorož, Slovenia, Aug./Sept. 2006, pp. 1099–1104.

[13] J. S. Lee, C.-H. Choi, J.-K. Seok, and R. D. Lorenz, "Deadbeat-direct torque and flux control of interior permanent magnet synchronous machines with discrete time stator current and stator flux linkage observer," *IEEE Trans. Ind. Appl.*, vol. 47, no. 4, pp. 1749–1758, July/Aug. 2011.

[14] T. Geyer, "Model predictive direct torque control: derivation and analysis of the state-feedback control law," *IEEE Trans. Ind. Appl.*, vol. 49, no. 5, pp. 2146–2157, Sept./Oct. 2013.

[15] L. Harnefors, K. Pietiläinen, and L. Gertmar, "Torque-maximizing field-weakening control: design, analysis, and parameter selection," *IEEE Trans. Ind. Electron.*, vol. 48, no. 1, pp. 161–168, Feb. 2001.

[16] O. Wallmark, S. Lundberg, and M. Bongiorno, "Input admittance expressions for field-oriented controlled salient PMSM drives," *IEEE Trans. Power Electron.*, vol. 27, no. 3, pp. 1514–1520, Mar. 2012.

[17] B.-H. Bae and S.-K. Sul, "A compensation method for time delay of full-digital synchronous frame current regulator of PWM AC drives," *IEEE Trans. Ind. Appl.*, vol. 39, no. 3, pp. 802–810, May/June 2003.

[18] G. F. Franklin, J. D. Powell, and M. Workman, *Digital Control of Dynamic Systems*, 3rd ed. Menlo Park, CA: Addison-Wesley, 1997.

[19] Z. Qu, T. Tuovinen, and M. Hinkkanen, "Inclusion of magnetic saturation in dynamic models of synchronous reluctance motors," in *Proc. ICEM'12*, Marseille, France, Sept. 2012, pp. 994–1000.

Marko Hinkkanen (M'06–SM'13) received the M.Sc.(Eng.) and D.Sc.(Tech.) degrees from Helsinki University of Technology, Espoo, Finland, in 2000 and 2004, respectively. Since 2000, he has been with Helsinki University of Technology (part of Aalto University, Espoo, since 2010). He is currently an Assistant Professor (tenure track) with the Aalto University School of Electrical Engineering. His research interests include control systems, electric drives, and power converters.

Zengcai Qu received the B.Sc. degree in electrical engineering and automation from Shanghai Jiao Tong University, Shanghai, China, in 2007 and the M.Sc. degree in space science and technology jointly from Lulea University of Technology, Kiruna, Sweden, and Helsinki University of Technology, Espoo, Finland, in 2009. Since 2009, he has been working towards the D.Sc.(Tech.) degree at Aalto University, Espoo. His research interests are efficiency control and sensorless control of electric drives.

Hafiz Asad Ali Awan received the B.Sc. degree in electrical engineering from University of Engineering & Technology, Lahore, Pakistan in 2012. Since 2013, he has been working towards his Masters degree in electrical engineering at Aalto University, Espoo, Finland. His main research interest is the control of electric drives.

Toni Tuovinen received the M.Sc. degree from the University of Helsinki, Helsinki, Finland, in 2005 and the M.Sc.(Eng.) degree from Helsinki University of Technology, Espoo, Finland, in 2009. He received the D.Sc.(Tech.) degree from Aalto University, Espoo, in 2014. He is currently a Senior Design Engineer with ABB Oy, Helsinki. His main research interests include the control of electric drives.

Fernando Briz (A'96–M'99–SM'06) received the M.S. and Ph.D. degrees from the University of Oviedo, Gijón, Spain, in 1990 and 1996, respectively. From June 1996 to March 1997, he was a Visiting Researcher with the University of Wisconsin, Madison. He is currently a Full Professor with the Department of Electrical, Computer and Systems Engineering, University of Oviedo. His topics of interest include control systems, power converters and ac drives, machine diagnostics and digital signal processing. Dr. Briz received the 2005 IEEE TRANSACTIONS ON INDUSTRY APPLICATIONS Third Place Prize Paper Award and was the recipient of five IEEE Industry Applications Society Conference and IEEE Energy Conversion Congress and Exposition prize paper awards. He is currently Program Chair and Associate Editor of the Industrial Drives Committee of the IAS-IPCSD.